

Dual-polarimetric descriptors from Sentinel-1 GRD SAR data for crop growth assessment

Narayanarao Bhogapurapu^{a,*}, Subhadip Dey^a, Avik Bhattacharya^a,
Dipankar Mandal^a, Juan M. Lopez-Sanchez^b, Heather McNairn^c,
Carlos López-Martínez^d, Y. S. Rao^a

^a*Microwave Remote Sensing Lab, Centre of Studies in Resources Engineering,
Indian Institute of Technology Bombay, Mumbai, India*

^b*University of Alicante, Alicante, Spain*

^c*Ottawa Research and Development Centre, Agriculture and Agri-Food Canada, Canada*

^d*Signal Theory and Communications Department (TSC), Universitat Politècnica de
Catalunya (UPC), Barcelona, Spain*

Abstract

Accurate and high-resolution spatio-temporal information about crop phenology obtained from Synthetic Aperture Radar (SAR) data is an essential component for crop management and yield estimation at a local scale. Crop growth monitoring studies seldom exploit complete polarimetric information contained in dual-pol GRD SAR data. In this study, we propose three polarimetric descriptors: the pseudo scattering-type parameter (θ_c), the pseudo scattering entropy parameter (H_c), and the co-pol purity parameter (m_c) from dual-pol S1 GRD SAR data. We also introduce a novel unsupervised clustering framework using H_c and θ_c with six clustering zones to represent various scattering mechanisms. We implemented the proposed algorithm on the cloud-based Google Earth Engine (GEE) platform for Sentinel-1 SAR data. We have shown the sensitivity of these descriptors over a time series of

*Corresponding author: N. Bhogapurapu (narayanarao.bhogapurapu@gmail.com)

data for wheat and canola crops at a test site in Canada. From the leaf development stage to the flowering stage for both crops, the pseudo scattering-type parameter θ_c changes by approximately 17° . Moreover, within the entire phenology window, both m_c and H_c varies by about 0.6. The effectiveness of θ_c and H_c to cluster the phenological stages for the two crops is also evident from the clustering plot. During the leaf development stage, about 90 % of the sampling points were clustered into the low to medium entropy scattering zone for both the crops. Throughout the flowering stage, the entire cluster shifted into the high entropy vegetation scattering zone. Finally, during the ripening stage, the clusters of sample points were split between the high entropy vegetation scattering zone and the high entropy distributed scattering zone, with $> 55\%$ of the sampling points in the high entropy distributed scattering zone. This innovative clustering framework will facilitate the operational use of S1 GRD SAR data for agricultural applications.

Keywords: GRD SAR, Dual-pol, phenology, Unsupervised clustering, GEE, Sentinel-1

1. Introduction

Synthetic Aperture Radar (SAR) data have been extensively used for crop growth monitoring and classification, yield estimation, and phenological stages characterization. This is due to their high sensitivity towards the structure and dielectric properties of crop canopies (Ulaby, 1975; Ulaby and El-Rayes, 1987; Brisco et al., 1992; Ferrazzoli et al., 1992; McNairn and Brisco, 2004; Steele-Dunne et al., 2017). Because of its high spatial resolution and all-weather capabilities, SAR has proven to be a promising data

9 source for continuously monitoring crops at field scales. The interaction of
10 the SAR signal with crop canopies and the underlying soil varies with wave-
11 length, polarization and angle of incidence (Ferrazzoli et al., 1992; Davidson
12 et al., 2000). In general, during the early vegetative growth stage, the SAR
13 backscatter signal is significantly affected by the underlying soil (Wiseman
14 et al., 2014). The canopy structure and canopy moisture distribution are
15 among major observable biophysical parameters that influence backscatter
16 at each phenological stage. Further, the dense and complex geometry of
17 the canopy leads to randomness in the scattering, which is more significant
18 for fully developed crop canopies (Mascolo et al., 2016; Hariharan et al.,
19 2018; Wang et al., 2019). The scattering becomes increasingly unpredictable
20 during fruit development stages, leading to greater randomness in the SAR
21 response (Jiao et al., 2014).

22 The availability of dual-pol SAR data acquired by the Sentinel-1 con-
23 stellation provides diverse opportunities for many crop monitoring applica-
24 tions (ESA, 2017). Compared to full-pol mode, dual-pol modes have ad-
25 vantages in terms of larger swath widths and lower data volumes, but at
26 the expense of reduced polarimetric information (Lee et al., 2001; Ainsworth
27 et al., 2009). The Sentinel-1 (S1) SAR sensor in Interferometric Wide (IW)
28 swath mode acquires data in dual-polarization, either in VV-VH or HH-HV.

29 Several researchers indicated the potential use of dual-pol backscatter
30 intensities for crop type identification (Kussul et al., 2016; Nguyen et al.,
31 2016; Bargiel, 2017; Van Tricht et al., 2018; Mandal et al., 2018; Whelen
32 and Siqueira, 2018; Minasny et al., 2019; Arias et al., 2020), crop biophysi-
33 cal parameter estimation (Bousbih et al., 2017; Kumar et al., 2018; Mandal

et al., 2020a), and phenology identification (Nelson et al., 2014; De Bernardis et al., 2015; Lasko et al., 2018; Singha et al., 2019; Fikriyah et al., 2019). Cloude (2007) proposed a clustering technique for dual-polarimetric (HH-HV or VV-VH) SAR data. An eigendecomposition of the 2×2 covariance matrix is performed to characterize scattering mechanisms from targets. The average scattering angle $\bar{\alpha}$ is obtained from the two orthogonal polarization states weighted by their corresponding pseudo probabilities obtained from the eigenvalues. The entropy H is obtained from the pseudo probabilities. Ainsworth et al. (2008) introduced a scattering-type parameter θ for dual-pol SLC data (HH-HV) utilizing the eigendecomposition technique. This parameter is presented as a measure between the cross- and co-pol backscatter ratio ($\sigma_{XY}^{\circ}/\sigma_{XX}^{\circ}$). It was stated that although the formulation is similar to Cloude α , the scattering information content is different. Utilizing θ and the scattering entropy (H) for dual-pol SAR data, an unsupervised clustering framework was proposed to identify different targets based on their scattering mechanisms. The unsupervised clustering plane was divided into eight different zones based on the scattering types.

Besides this, several vegetation descriptors such as the Radar Vegetation Index (RVI) for dual-pol (Trudel et al., 2012), Dual-Pol SAR Vegetation Index (DPSVI) (Periasamy, 2018), and Dual-pol Radar Vegetation Index (DpRVI) (Mandal et al., 2020b) have been developed for crop growth monitoring and biophysical parameter retrieval. However, similar descriptors are not directly available for dual-pol GRD SAR data products.

In particular, investigation often is limited to the direct use of backscatter intensities or their ratios for crop phenology identification and cluster-

ing. Vreugdenhil et al. (2018) studied the sensitivity of backscatter intensities and the cross-pol ratio (VH/VV) to crop biophysical parameters such as the Vegetation Water Content (VWC), Leaf Area Index (LAI), biomass, and the plant height for three different crops using the Sentinel-1 GRD SAR data.

Temporal sensitivity analysis using various machine learning models has shown that the cross-pol ratio is a valuable parameter for monitoring crop biophysical parameters and phenology. Song and Wang (2019) analyzed the temporal trend of VV and VH backscatter intensities to identify and map winter wheat crop using a parallelepiped classifier. They distinguished different phenology stages by exploring the temporal trend of the VH/VV ratio and its slope.

Nasrallah et al. (2019) fitted multiple Gaussian functions to a time-series of backscatter intensities (VV, VH and VH/VV) to estimate the date of significant phenology stages for wheat. Wali et al. (2020) explored the sensitivity of temporal backscatter intensities of rice biophysical parameters using a combination of linear regression lines. With this approach, they were able to identify the reproductive growth stages of rice. Schlund and Erasmi (2020) demonstrated the sensitivity of interferometric phase information to estimate the dates of different phenology stages of wheat.

Information about phenological status can increase crop classification accuracy (Bargiel, 2017; Li et al., 2019). However, available studies on crop monitoring using GRD SAR data are mostly limited to the direct use of backscatter intensities and their ratios, along with a few empirical models. These approaches partly utilize the available polarimetric information from dual-pol GRD SAR data. Dual-polarimetric descriptors that characterize

84 different target scattering mechanisms have a wide range of applicability
85 compared to empirical and data-driven models limited to specific crops and
86 regions. In this regard, an unsupervised clustering framework that suitably
87 utilizes the available polarimetric information from dual-pol GRD SAR data
88 is needed to monitor crop growth dynamics.

89 In general, polarimetric parameters have been directly attributed to the
90 physical properties of the crop canopy (Lopez-Sanchez et al., 2012, 2014;
91 McNairn et al., 2018; Dey et al., 2020b), and has therefore helped monitor
92 crop phenology. Unfortunately, the polarimetric parameters reported in these
93 studies are not immediately apparent in the case of dual-pol GRD SAR data.

94 The majority of SAR-based crop monitoring studies were limited to small
95 study areas due to the high volume of data processing. For example, the
96 Sentinel-1 constellation acquires data at a rate of approximately 600 GB per
97 day (Ali et al., 2017). This volume of data requires high storage and compu-
98 tational resources for processing. Unfortunately, these resources are limited
99 and restricted for full exploitation to those with access to High-Performance
100 Computing Systems (HPCS). With the advent of cloud platforms such as the
101 Google Earth Engine (GEE) (Gorelick et al., 2017), the NASA Earth Ex-
102 change (Nemani et al., 2011), Amazon Web Services (AWS) (Jackson et al.,
103 2010), and Microsoft Azure (Redkar et al., 2009), large-scale remote sensing
104 and geospatial data analysis have become possible with minimum local com-
105 putational resources (Hird et al., 2017). In this aspect, the web-based GEE
106 platform is designed to make planetary-scale remote sensing data process-
107 ing manageable and efficient (Gorelick et al., 2017). The free-to-use policy
108 and various in-built GEE algorithms make it an ideal tool for both experts

109 and non-experts alike. The major contributions of the current study are as
110 follows:

- 111 • Introduces three new dual-polarimetric descriptors: m_c , θ_c , and H_c .
- 112 • Proposes a new unsupervised clustering framework using two param-
113 eters (θ_c and H_c) obtained from the dual-pol GRD SAR data.
 - 114 – Six feasible clustering zones depicting different scattering mecha-
115 nisms.
 - 116 – Specific to crop monitoring, the proposed clustering framework
117 effectively characterizes different phenological stages.
- 118 • Demonstrates how the proposed algorithm is implemented on GEE,
119 making it available for global monitoring with minimal local computa-
120 tional requirements.

121 The performance of the parameters and clustering framework is analyzed
122 using time-series Sentinel-1 SAR data for monitoring wheat and canola.

123 2. Study area and dataset

124 The test site is located near Carman, Manitoba (Canada), covering an
125 intensively cropped area of $26 \text{ km} \times 48 \text{ km}$. The dominant crops grown in
126 this region include wheat, canola, soybeans, corn and oats, along with a small
127 fraction of acreages in grassland and pasture. The sowing period of crops in
128 this region varies from early to late May, depending on crop variety and
129 cultivation practices. The harvesting period extends until late September.

130 The nominal size of each field is approximately $800\text{ m} \times 800\text{ m}$. Each field
131 comprises 16 sampling locations arranged in two parallel transects separated
132 by 200 m, as shown in Figure 1. During the SMAPVEX-16 campaign, in-situ
133 measurement of vegetation and soil was collected for 50 fields near coincident
134 with satellite acquisitions.

135 In this study, we have considered 24 fields (13 wheat and 11 canola) for
136 analysis. Figure 1 presents the distribution of the selected fields in the study
137 area. One can find additional details regarding in-situ sampling methods
138 during the SMAPVEX-16 campaign in McNairn et al. (2016); Bhuiyan et al.
139 (2018).

140 Figures 2 and 3 provide field photos of different growth stages of wheat
141 and canola, respectively. The Manitoba weekly agriculture reports Agriculture
142 (2016) provide additional details regarding crop conditions. Sentinel-
143 1 operates at C-band with a central transmit frequency of 5.405 GHz. In
144 this work, we have utilized the data acquired with the Interferometric Wide
145 swath (IW) mode with a swath width of 250 km. The spatial resolution is
146 $5\text{ m} \times 20\text{ m}$ in range and azimuth, respectively, and the Noise Equivalent
147 Sigma Zero (NESZ) is -25 dB with the incidence angle varying between 20°
148 to 46° . From the available Sentinel-1 images acquired during the campaign,
149 we have used eight dual-pol (VV-VH) C-band Sentinel-1A GRD SAR in the
150 present study. We have utilized the VV-VH data acquired with IW mode
151 with incidence angle ranging from 30.65° to 41.76° . Complete details of the
152 SAR data utilized in the study are presented in Table 1.

153 The data were chosen based on the availability of in-situ measurements
154 of crop phenology stages and coincident Sentinel-1A acquisitions for six days

of the year (DOY) for wheat (DOY-146, 165, 182, 189, 201, 230) and canola
(DOY-146, 165, 182, 189, 206, 225).

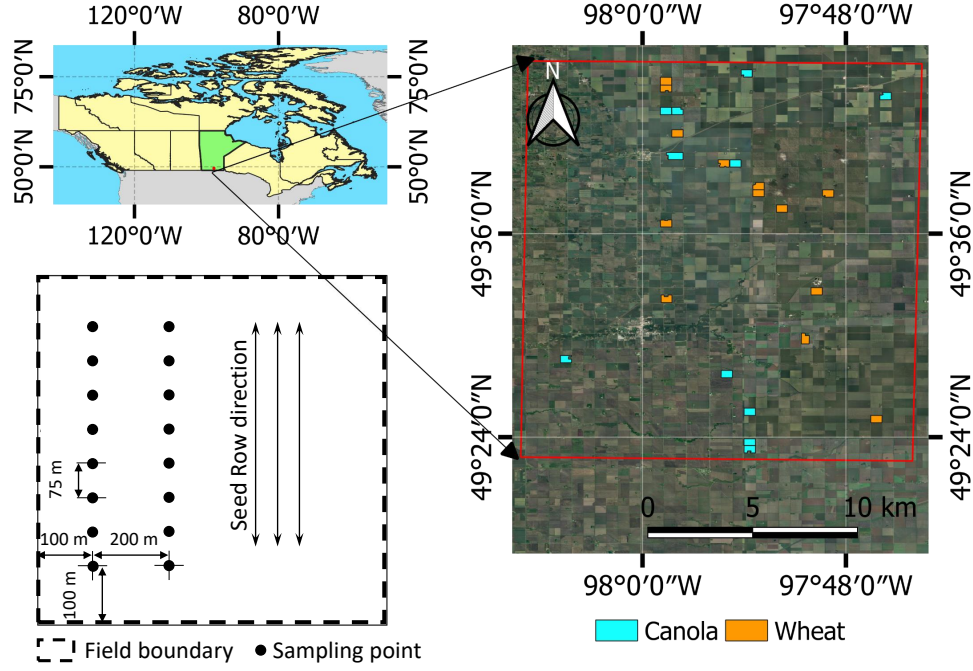


Figure 1: The study area and the distribution of wheat and canola fields in the study area overlaid on a Google earth image. The sampling schema followed for ground truth collection is detailed in the dashed rectangle (bottom left).

3. Methodology

This section proposes three descriptors from the Level-1 S1 GRD SAR data. We express the co-pol purity parameter in terms of the co-pol to cross-pol ratio, which is then used to obtain the scattering-type parameter. The measure of scattering randomness is expressed in terms of the ratio parameter. We utilize these descriptors to introduce a clustering framework

Table 1: Details and specification of Sentinel-1A data used in the present study. Data are acquired from the Carman test site during the SMAPVEX16-MB campaign. The range of incidence angles shown is specific to the location of the sample sites (IW: Interferometric Wide swath)

Date	DOY	Acquisition Mode	Incidence angle range (deg.)	Orbit
25-May-16	146	IW	40.18 - 41.76	Ascending
13-Jun-16	165	IW	30.65 - 32.70	Ascending
30-Jun-16	182	IW	40.17 - 41.75	Ascending
07-Jul-16	189	IW	30.64 - 32.69	Ascending
19-Jul-16	201	IW	30.70 - 32.70	Ascending
24-Jul-16	206	IW	40.16 - 41.74	Ascending
12-Aug-16	225	IW	30.65 - 32.70	Ascending
17-Aug-16	230	IW	40.16 - 41.74	Ascending

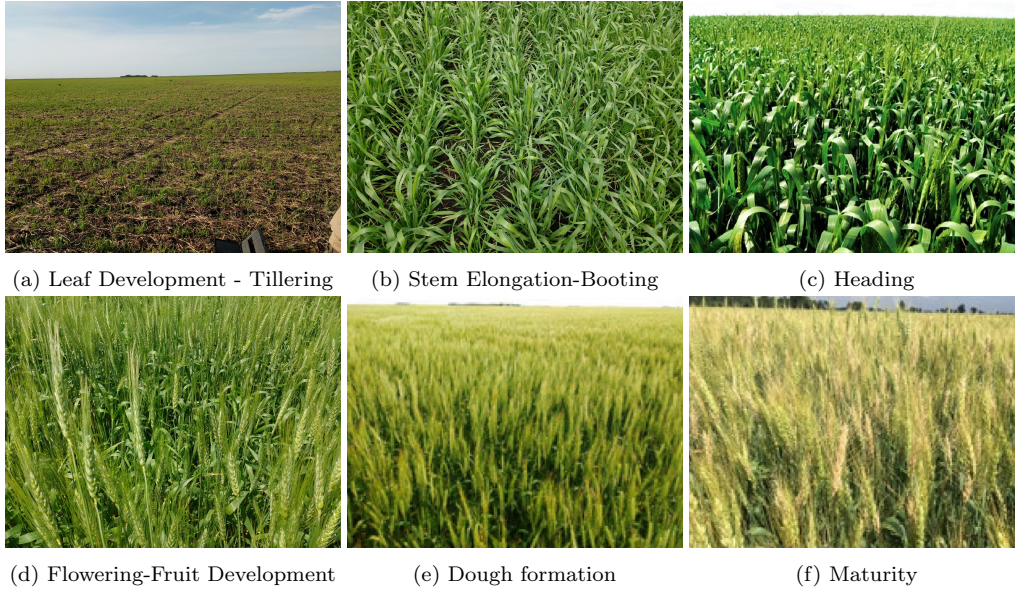


Figure 2: Field photos showing different phenology stages of wheat.

for crop phenology identification. Finally, we present the overall processing
chain of the framework using the GEE platform.



Figure 3: Field photos showing different phenology stages of canola.

3.1. Dual-polarimetric descriptors

In this section, we present three dual-polarimetric descriptors from the Level-1 S1 GRD SAR data. We propose an unsupervised clustering framework to monitor different crop growth stages based on their diverse scattering characteristics using these descriptors. In the Level-1 S1 GRD SAR data product, we obtain backscatter response either in $(\sigma_{VV}^{\circ}, \sigma_{VH}^{\circ})_{dB}$ or $(\sigma_{HH}^{\circ}, \sigma_{HV}^{\circ})_{dB}$ modes, where H and V are respectively the horizontal and vertical transmit and receive polarization components. The subscript dB represents the GRD SAR data products in decibel (dB) scale. In general, for a monostatic antenna configuration and a natural scene, we assume $\sigma_{XY}^{\circ} \leq \sigma_{XX}^{\circ}$ (where X and Y are H or V polarizations respectively) (Cloude, 2009). Using this assumption, we consider the ratio parameter, $0 \leq q = \frac{\sigma_{XY}^{\circ}}{\sigma_{XX}^{\circ}} \leq 1$, in the linear scale. This parameter has been widely used in the literature as a descriptor for

several crop monitoring applications (Della Vecchia et al., 2008; Vreugdenhil et al., 2018; Homayouni et al., 2019). In the GRD product, we do not keep the relative phase information between the XX and XY polarization. Hence, we cannot obtain covariance information from the GRD product, unlike the SLC data. We express the co-pol purity parameter (m_c) in terms of q given in Equation 1. It can be noted that for $q = 1$, $m_c = 0$, and for $q = 0$, $m_c = 1$. In between these two extreme cases, $1 > q > 0$, $0 < m_c < 1$.

$$m_c = \frac{1 - q}{1 + q}; \quad 0 \leq m_c \leq 1 \quad (1)$$

Utilizing σ_{XX}° , σ_{XY}° , and m_c we define two auxiliary quantities as,

$$\tan \zeta_1 = \frac{\sigma_{XX}^\circ}{m_c I} \quad \text{and} \quad \tan \zeta_2 = \frac{\sigma_{XY}^\circ}{m_c I}, \quad (2)$$

where the total intensity, $I = \sigma_{XX}^\circ + \sigma_{XY}^\circ$. By using a simple relationship, we obtain,

$$\begin{aligned} \tan \theta_c &= \tan (\zeta_1 - \zeta_2) \\ &= \frac{(1 - q)^2}{1 + q^2 - q}; \quad 0^\circ \leq \theta_c \leq 45^\circ \end{aligned} \quad (3)$$

We can observe from equation (3) that when $m_c = 0$, then $\theta_c = 0^\circ$ characterizes complex scattering from targets. Whereas, when $m_c = 1$, then $\theta_c = 45^\circ$, characterizes pure scattering from deterministic targets (i.e., trihedral or dihedral). Therefore, the pseudo scattering-type parameter $\theta_c \in [0^\circ, 45^\circ]$ characterizes different scattering information in between these two cases.

193 Next, we define the pseudo scattering entropy parameter as,

$$H_c = - \sum_{i=1}^2 p_i \log_2 p_i; \quad 0 \leq H_c \leq 1 \quad (4)$$

194 where $p_1 = \frac{1}{1+q}$ and $p_2 = \frac{q}{1+q}$ are the two pseudo probability measures
 195 with $p_1 \geq p_2$. We can observe that $H_c = 1$ for $p_1 = p_2$ (i.e., $q = 1$), whereas
 196 $H_c = 0$ for $p_1 = 1$ (i.e., $q = 0$).

197 Using θ_c and H_c together, we propose an unsupervised clustering frame-
 198 work shown in Fig. 4. The curve (Curve I) represents the unique feasible
 199 clustering section in the H_c/θ_c plot. It can be noted that this curve is deter-
 200 mined from the theoretical relationship between θ_c and H_c while varying m_c
 between 0 to 1.

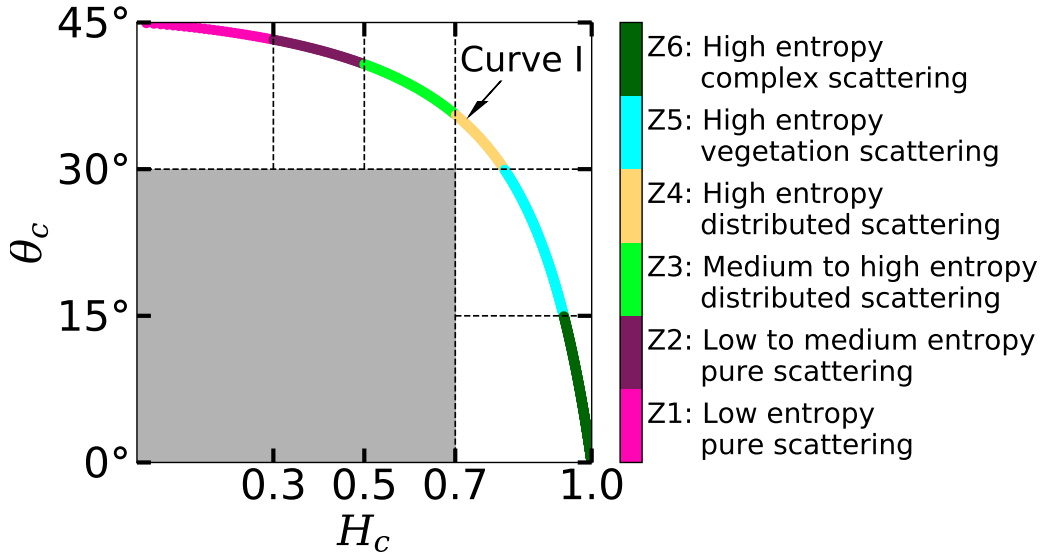


Figure 4: The H_c/θ_c 2D clustering sections. The curve is divided into six zones: Z1 to Z6.

201

202 Based on particular scattering characteristics from targets (Cloude and
 203 Pottier, 1997), we propose six possible clustering zones: Z1, Z2, Z3, Z4, Z5

204 and Z6 by splitting H_c into four sub-categories: $[0, 0.3)$, $[0.3, 0.5)$, $[0.5, 0.7)$,
 205 and $[0.7, 1.0]$, and θ_c into three sub-categories: $[0^\circ, 15^\circ)$, $[15^\circ, 30^\circ)$, $[30^\circ, 45^\circ]$.
 206 Each of these zones represents different scattering phenomena from the scene.
 207 The relationship between q and the three proposed descriptors (θ_c , m_c , and
 208 H_c) along with the boundary values of the clustering zones is shown in Fig-
 209 ure 5 and Table 2.

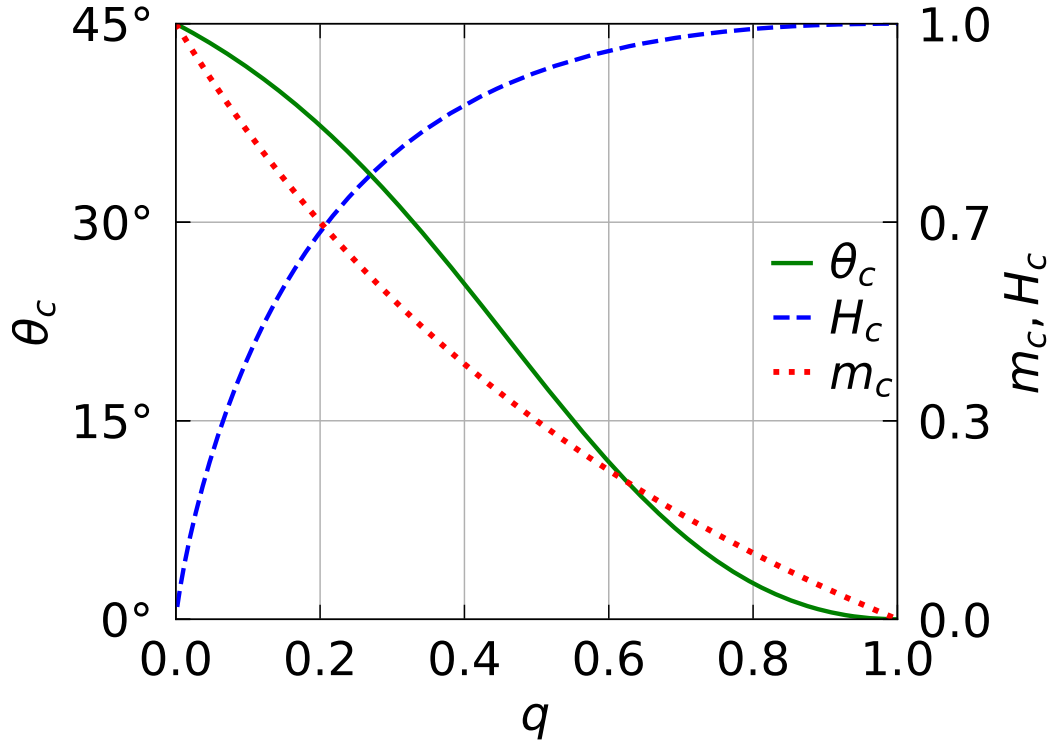


Figure 5: Relationship between the proposed descriptors (θ_c , m_c , H_c) and q .

210 Cloude (2007) proposed the $H/\bar{\alpha}$ clustering technique for dual-polarimetric
 211 (HH-HV or VV-VH) SAR data. Unlike full-polarimetric measurements, the
 212 2×2 covariance matrix is formed using only the column of the scattering ma-
 213 trix to characterize various targets. The scattering angle α is obtained from
 214 the eigenvector parameterization, and H is obtained from the eigenvalues of

Table 2: Boundary values of the descriptors (H_c , θ_c , q , and m_c) for adjacent zones in the proposed clustering framework

	H_c	θ_c	q	m_c
—	0	45°	0	1
Z1–Z2	0.30	43.25°	0.06	0.89
Z2–Z3	0.50	40.74°	0.12	0.78
Z3–Z4	0.70	35.59°	0.23	0.62
Z4–Z5	0.81	30.00°	0.33	0.51
Z5–Z6	0.94	15.00°	0.55	0.29
—	1	0°	1	0

the covariance matrix as pseudo probabilities. The average scattering angle $\bar{\alpha}$ is obtained from the two orthogonal polarization states weighted with the two corresponding pseudo probabilities.

It is important to note that we cannot directly apply the $H/\bar{\alpha}$ decomposition technique to characterize target scattering mechanisms for GRD SAR data. Hence, to characterize targets utilizing GRD data, we propose an equivalent scattering angle θ_c based on the approach presented in (Dey et al., 2020a). We present the comparison of the two scattering angles for elementary targets and volume scattering models from a random cloud of anisotropic particles in Table 3. For comparison purpose, the scattering angle θ_c is scaled to the same range of $\bar{\alpha}$ as, $\bar{\theta}_c = 45^\circ - \theta_c$. We can note that all elementary targets reside at the origin, whereas the volume scattering models reside precisely on the lower curve of the $H/\bar{\alpha}$ plane.

Unlike the unsupervised clustering plane formed from the dual-pol H/α framework, the proposed H_c/θ_c framework forms a clustering segment. Both θ_c and H_c are derived from the cross-pol ratio q . However, their physical interpretations for targets are quite different due to their fundamental formula-

Table 3: Comparison between Cloude $\bar{\alpha}$ and $\bar{\theta}_c$ for elementary targets and volume scattering models for dual-polarimetric SAR data.

	Trihedral	Dihedral	Prolate	Oblate	Noise (Identity)
$\bar{\alpha}$	0°	0°	22.5°	10°	45°
$\bar{\theta}_c$	0°	0°	15.3°	4.3°	45°
$H = H_c$	0	0	0.811	0.503	1

tion, even though there is some correlation between the two parameters. On the one hand, the derivation of H_c is equivalent to the von Neumann type of entropy (represented as Shannon entropy) utilizing the pseudo-probabilities in terms of q . On the other hand, the derivation of θ_c follows from the equivalent formalism given in (Dey et al., 2020a). It characterizes scattering-type information using co-pol purity (m_c) and total intensity (I) in terms of q . One can note that their combined use is also supported by a better separation of clusters when the thresholds are defined by any one of these parameters.

The division of the clustering segment is realized from the symmetry relation for the scattering of a polarized wave. The input Stokes vector \mathbf{S}_i and output Stokes vector to the scattering medium \mathbf{S}_o are related by a linear relation of the form: $\mathbf{S}_o = \mathbf{K}\mathbf{S}_i$. Several restrictions are attributed to the Kennaugh matrix \mathbf{K} depending upon the symmetry and reciprocity requirements. Scattering from symmetrical medium makes \mathbf{K} diagonal. In the limit of weak scattering, the linear response of the scattering medium is determined by the ensemble-averaged covariance satisfying the Bethe-Salpeter equation (Cloude and Pottier, 1997). Following some rigorous computation, \mathbf{S}_o can be expressed as a function of the number of scattering events, n . Having specified \mathbf{S}_o , we can formulate the expression of the degree of polarization, m

251 in terms of n . From the definition of entropy S (H_c in this context) given in
 252 (Brosseau, 1991; Bicout and Brosseau, 1992), which is a function of the de-
 253 gree of polarization m , satisfying the inequality: $S(m = 1) \leq S \leq S(m = 0)$.
 254 Therefore, we observe that S increases with increase in n , as, $S(n = 0) = 0$;
 255 $S(n = 1) \approx 0.3$; $S(n = 2) \approx 0.5$, and, $S(n \geq 3) \approx 0.7$, and further increas-
 256 ing n (i.e., higher-order scattering), S saturates for both dual- and full-pol
 257 case. Furthermore, for dual cross-pol case, $H_c \approx 0.7$ for randomly oriented
 258 cylinders. A similar dependency of the scattering-type parameter (Cloude
 259 α) can also be observed as a function of the order of scattering n . We can
 260 approximately translate this observation to θ_c .

261 3.2. *Effect of system parameters on the proposed descriptors*

262 In this section, we show the analysis of the effect of polarization com-
 263 bination and frequency. Also, we present a comparative study of conven-
 264 tional dual-pol descriptors from SLC data and the proposed dual-pol de-
 265 scriptors from dual-pol GRD SAR data. In this context, we have utilized
 266 the RADARSAT-2 (C-band) and UAVSAR (L-band) data acquired over a
 267 Canadian test site for wheat. During the acquisition, wheat was at flowering
 268 to heading stage. The sampling points consists of acquisitions from two dates
 269 (29 June 2012 and 14 July 2012), and the incidence angle ranges from 22.2°
 270 to 26.5° .

271 We know that longer wavelength SAR signal (L-band) penetration depth
 272 is higher than the shorter SAR signal (C-band). Moreover, a shorter wave-
 273 length SAR signal (C-band) will suffer relatively more attenuation within
 274 vegetation canopies than a longer wavelength SAR signal (L-band). There-
 275 fore, we observe the differences in the proposed descriptors for different in-

276 cident frequencies. From Table 4, we can observe higher values of m_c and
 277 lower values of the pseudo scattering entropy in the case of L-band compared
 278 to the C-band. It may be due to less attenuation of the L-band compared
 279 to C-band. Similarly, we observe that the values of θ_c are more towards a
 280 pure scattering-type in the L-band than the C-band in both the dual-pol
 281 combinations. Also, we observe some effects of polarization combination on
 282 the descriptors. The predominantly vertical structure of the wheat canopy
 283 leads to higher interaction of the V-pol than the H-pol. Hence, we observe
 284 higher scattering entropy H_c and lower co-pol purity m_c in the VV+VH
 285 combination.

286 Besides, we observed higher values of the scattering-type parameter θ_c in
 287 the HH+HV combination than the VV+VH combination. The high value
 288 of θ_c indicates that the scattering mechanism is comparatively purer in the
 289 HH+HV combination than the VV+VH combination due to less interaction
 290 of H-pol with the vertically oriented crop canopy than the V-pol.

Table 4: Effect of frequency on the proposed dual-pol descriptors for wheat.

Frequency	HH+HV			VV+VH		
	m_c	H_c	θ_c	m_c	H_c	θ_c
C-band (5.405 GHz)	0.79 ± 0.08	0.47 ± 0.12	$40.78^\circ \pm 2.30^\circ$	0.53 ± 0.12	0.78 ± 0.1	$30.33^\circ \pm 6.59^\circ$
L-band (1.258 GHz)	0.93 ± 0.03	0.22 ± 0.07	$43.84^\circ \pm 0.59^\circ$	0.83 ± 0.08	0.4 ± 0.14	$41.79^\circ \pm 2.15^\circ$

291 A comparative study between the conventional SLC dual-pol descriptors:
 292 Barakat degree of polarization m , scattering entropy H and Cloude $\bar{\alpha}$, and
 293 the proposed GRD dual-pol descriptors: co-pol purity m_c , pseudo scattering-
 294 entropy H_c , and pseudo scattering-type parameter θ_c . Table 5 shows the
 295 values of the conventional dual-pol descriptors and the proposed descriptors
 296 for two dual-pol combinations for the above experiment setup. We observe

297 a negligible difference between H and H_c , and m and m_c . However, we
 298 observe a noticeable difference between the scattering-type parameters, $\bar{\alpha}$
 299 and $\bar{\theta}_c$ (kindly note that $\bar{\theta}_c = 45^\circ - \theta_c$). This difference could be because of
 300 the parameterization of the eigenvector of the \mathbf{C}_2 matrix while deriving the
 301 Cloude α . Hence, we can say that our proposed parameters obtained from
 302 dual-pol GRD SAR data possess equivalent information as the conventional
 303 parameters derived from dual-pol SLC data.

Table 5: Comparison of conventional dual-pol descriptors from SLC data and the proposed dual-pol descriptors from dual-pol GRD SAR data.

Channels	SLC			GRD		
	m	H	$\bar{\alpha}$	m_c	H_c	$\bar{\theta}_c$
HH+HV	0.80 ± 0.08	0.45 ± 0.15	$12.23^\circ \pm 4.24^\circ$	0.79 ± 0.08	0.47 ± 0.12	$4.22^\circ \pm 2.3^\circ$
VV+VH	0.55 ± 0.11	0.76 ± 0.10	$24.27^\circ \pm 5.45^\circ$	0.53 ± 0.13	0.78 ± 0.10	$14.67^\circ \pm 6.59^\circ$

304 3.3. Sentinel-1 dual-pol descriptors in GEE

305 This section describes the extraction process of the proposed polarimetric
 306 descriptors from the Sentinel-1 dual-pol GRD SAR data on the GEE plat-
 307 form. The overall processing framework comprises three major blocks: data
 308 preparation, clustering and temporal analysis, as shown in Figure 6.

309 In the data preparation block, we import the Level-1 Ground Range De-
 310 tected (GRD) Sentinel-1 backscatter coefficient (i.e., σ° in decibel) data into
 311 the GEE platform. The imported temporal data stack is cloud filtered using
 312 three filters:

- 313 • Metadata filter (bands: VV, VH, incidence angle, instrument mode:
 314 IW, and orbit: ascending)
- 315 • Temporal filter (date range: 25 May 2016 to 17 August 2016)

- Spatial bound filter (region of interest: shapefile of the study area)

Subsequently, we use two masks to generate a valid pixel data stack. As described in section 3.1, the first mask (i.e., $\sigma_{VV}^{\circ} > \sigma_{VH}^{\circ}$) ensures estimation constraints of the proposed descriptors, whereas the second mask (i.e., $\sigma_{VV}^{\circ} > -20$ dB) separates out water bodies. The backscatter values in the valid pixel data stack are then converted into a linear scale. Further, we use a 5×5 boxcar filter to despeckle the data.

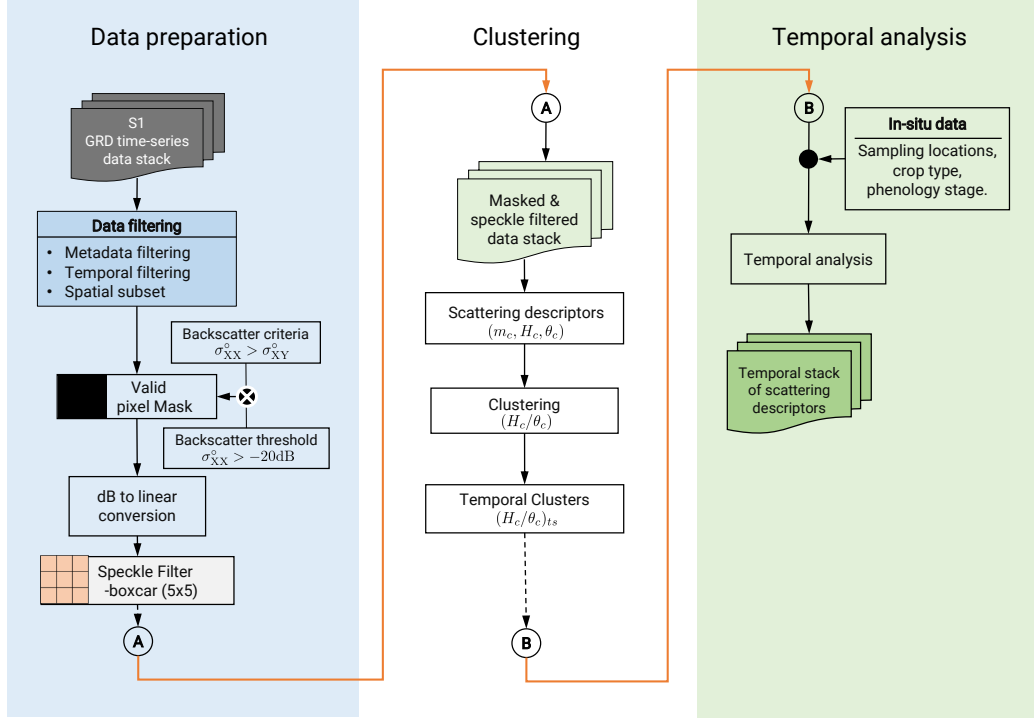


Figure 6: The proposed schematic workflow to derive the dual-polarimetric descriptors from Sentinel-1 dual-pol GRD SAR data on the GEE platform.

322

323 In the clustering block, we first generate the dual-pol descriptors using
 324 the Equations 1- 4 from the valid and speckle filtered data stack. Further,
 325 we utilize these descriptors to generate the H_c/θ_c clusters for each scene in

the temporal stack. The temporal analysis block starts by importing in-situ data such as sampling locations, crop type and crop phenology stages. Subsequently, we utilize these data to analyze the temporal stack of dual-pol descriptors and the H_c/θ_c clusters. Further, to complement the analysis, we generate temporal maps of each descriptor over the study area.

4. Results and discussion

In this section, we analyze the temporal dynamics of crops using the proposed dual-polarimetric descriptors. Furthermore, we utilize the proposed clustering framework to assess the phenological stages of the two crops (wheat, canola) from the C-band Sentinel-1 dual-pol GRD SAR data. The description of the phenological stages for wheat and canola are presented in Tables 6 and 7 respectively.

Table 6: Phenology stages of wheat. The BBCH (**B**iologische **B**undesanstalt, **B**undessortenamt und **C**hemische Industrie) codes of each phenology stage are also highlighted.

Phenology stage	BBCH code	Description
Leaf development	10-19	1-9 or more leaves unfolded
Tillering	20-29	Formation of 1-9 or more number of tillers
Stem elongation	30-39	Elongation of first internode to fully unrolled flag leaf
Booting	41-49	Flag leaf sheath extended to first awns visible
Heading	51-59	First spikelet to completely emerged heads
Flowering-fruit development	61-77	Beginning of flowering and formation of grains with milk
Doughstage	83-89	Development of soft to Hard dough
Maturity	92-97	Grain turns very hard and over ripened; grain loosening in day-time

4.1. Temporal dynamics of the dual-polarimetric descriptors

In this section, we present the temporal analysis of m_c , θ_c and H_c across the phenological stages of wheat and canola over Carman, Manitoba, Canada. The spatio-temporal changes of m_c , θ_c and H_c are shown in Figure 7, Figure 8, and Figure 9, respectively, over the entire test site. Variations for

Table 7: Phenology stages of canola. The BBCH (**B**iologische **B**undesanstalt, **B**undessortenamt und **C**hemische Industrie) codes of each phenology stage are also highlighted.

Phenology stage	BBCH code	Description
Leaf development	10-19	1-9 or more leaves unfolded
Side shoot formation	20-29	Formation of 1-9 or more side shoots
Stem elongation	30-39	Formation of 1-9 or more extended internodes
Inflorescence emergence	50-59	Formation of flower buds, still enclosed by leaves
Flowering	60-69	Starting from first flower opening to the majority of petals fallen
Pod development	71-79	Formation of pods and reaching their full size
Ripening	80-89	Green seeds hardens and turns into dark

all three parameters are evident with crop growth starting from early leaf development to maturity for most agricultural fields. We also present the temporal dynamics of H_c/θ_c clusters as shown in Figure 10, to assess the crop growth condition.

On DOY-146, most wheat and canola fields show high values of m_c (wheat: 0.81 ± 0.08 and canola: 0.82 ± 0.08), θ_c (wheat: $41.37^\circ \pm 2.04^\circ$ and canola: $41.6^\circ \pm 1.91^\circ$) and medium to low value of H_c (wheat: 0.43 ± 0.12 and canola: 0.42 ± 0.13). These responses are due to the minimal crop cover, before significant vegetative growth and leaf development. Hence, the soil characteristics (i.e., moisture and surface roughness) dominate the backscatter response. Therefore, the effect of soil roughness on the backscatter response is significant (Wiseman et al., 2014), which may have led these sample pixels to cluster in the low to medium entropy pure scattering zones (viz., Z1, Z2) in the H_c/θ_c map (Figure 10).

With crop growth advancing to the inflorescence stage, we observe an overall decrease in the values of m_c , which is evident in Figure 7. Thus, on DOY-206, we observe medium to low values of m_c (wheat: 0.43 ± 0.07 and canola: 0.42 ± 0.1). From the flowering to maturity stage, the canopy

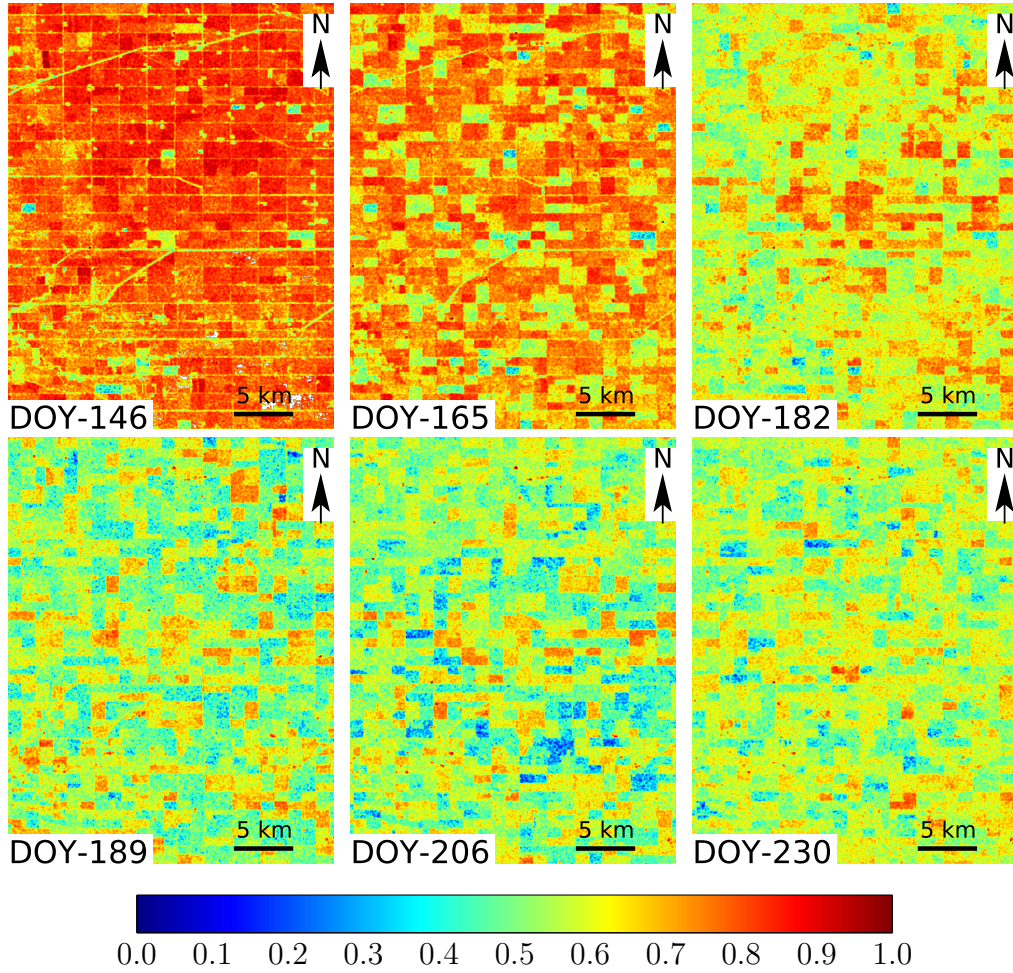


Figure 7: Temporal variation of m_c over the study area.

density increases as crop biomass increases (Wiseman et al., 2014; Hariharan et al., 2018). Therefore, as reported in (Sarabandi, 1991; Wang et al., 2019; Ratha et al., 2019), we also observe similar high scattering randomness at this stage.

Moreover, during this period, the observed backscatter response is expected to be dominated by the upper canopy layer. Additionally, the values

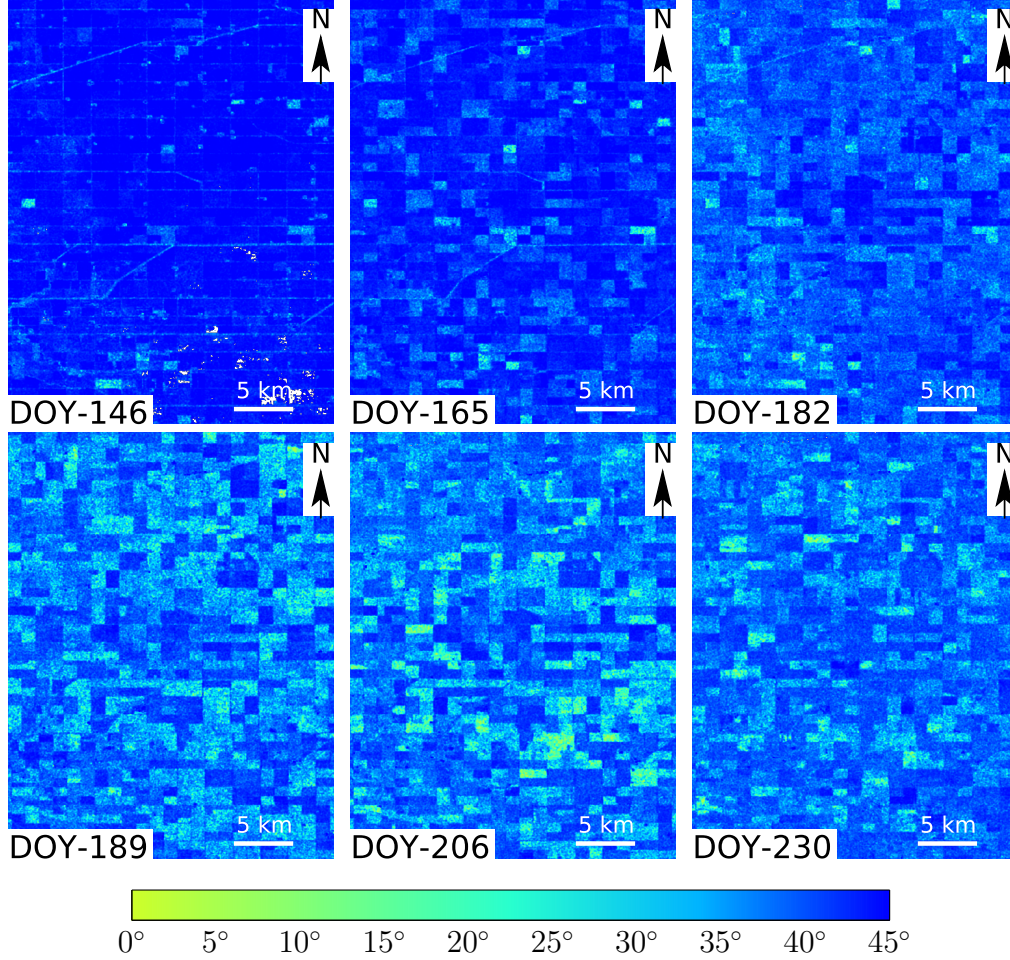


Figure 8: Temporal variation of pseudo scattering type parameter (θ_c) over the study area.

367 of θ_c for wheat are $24.51^\circ \pm 6.34^\circ$, and for canola $25.23^\circ \pm 4.7^\circ$ (Figure 8).
 368 These values are indicative of low random scattering within the resolution
 369 cells. We also observe an increasing trend of H_c due to the randomly oriented
 370 canopy structure. The values of H_c for wheat and canola are 0.86 ± 0.06
 371 and 0.86 ± 0.05 , respectively (Figure 9). Due to randomness in the vegeta-
 372 tion structure on DOY-206, we observe dominance within the high entropy
 373 vegetation scattering zone (Z5) in Figure 10.

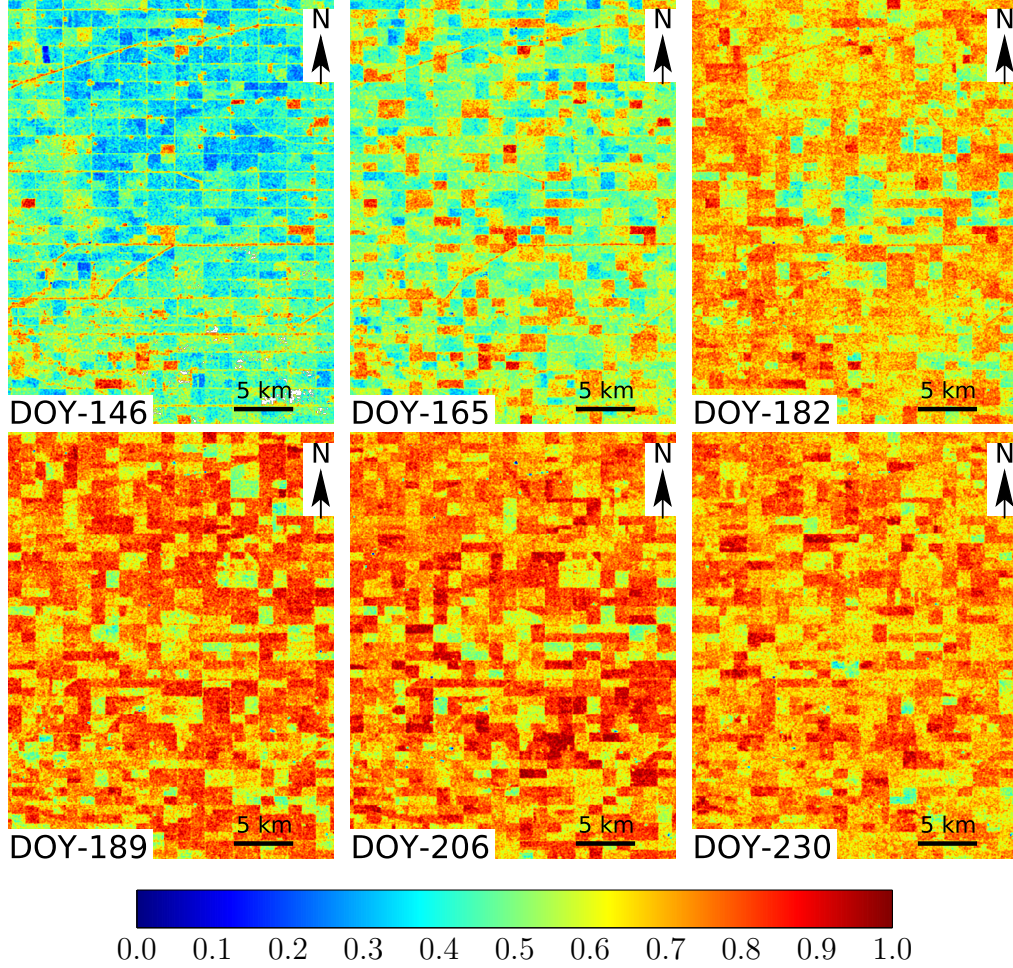


Figure 9: Temporal variation of pseudo scattering entropy parameter (H_c) over the study area.

One can note that all three polarimetric descriptors show a trend reversal at early crop senescence. This change could be due to the randomness variation corresponding to morphology attributes with a likely decrease in canopy moisture. We can observe from Figure 7 that m_c significantly increases during the ripening stage (DOY-230). At this stage, the values of m_c for wheat and canola are 0.52 ± 0.08 and 0.55 ± 0.08 , respectively. A similar trend is

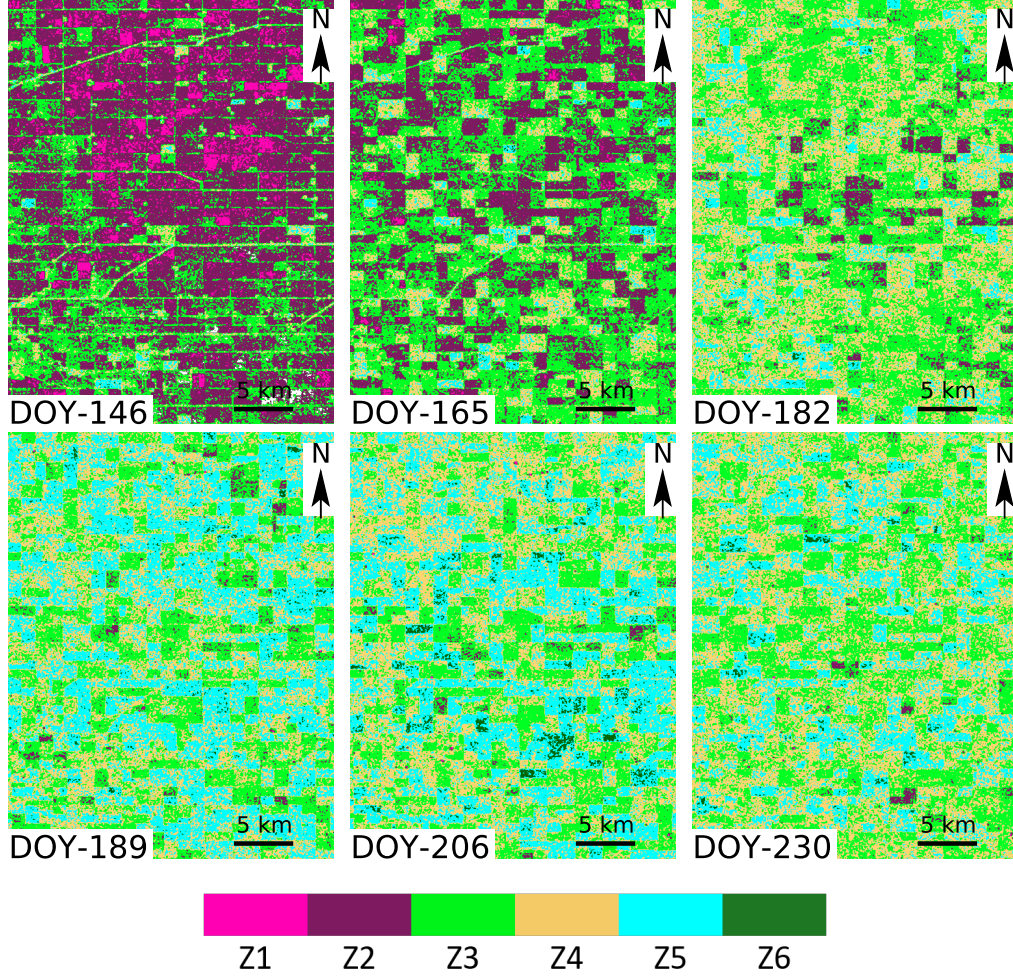


Figure 10: Temporal variation of H_c/θ_c clusters over the study area.

380 also observed for θ_c and H_c from Figures 8 and Figure 9. These notable
 381 changes in the polarimetric descriptors might be due to the enhanced ability
 382 of the radar wave to penetrate into the moderately dry crop canopy. Also,
 383 the vegetation water content variations might have decreased the SAR signal
 384 attenuation within the resolution cell.

385 4.2. Analysis over sampling fields

386 In the following sections, we provide a detailed quantitative analysis of
 387 the three descriptors (m_c , θ_c , and H_c) and the novel clustering framework for
 388 wheat and canola. In this study, we considered a total of 24 sample fields
 389 (wheat: 13 and canola: 11) for sensitivity and performance evaluation of the
 390 descriptors during temporal morphological changes in the canopies.

391 4.2.1. Wheat

392 First, we analyse temporal characteristics of m_c , H_c and θ_c for different
 393 phenological stages of wheat. We considered a total of 48 sampling points in
 394 three different fields (Field no. 62, 220, and 233) for assessing the temporal
 395 dynamics of θ_c , H_c and m_c . We also evaluate temporal variations of the
 396 H_c/θ_c clusters according to wheat phenology.

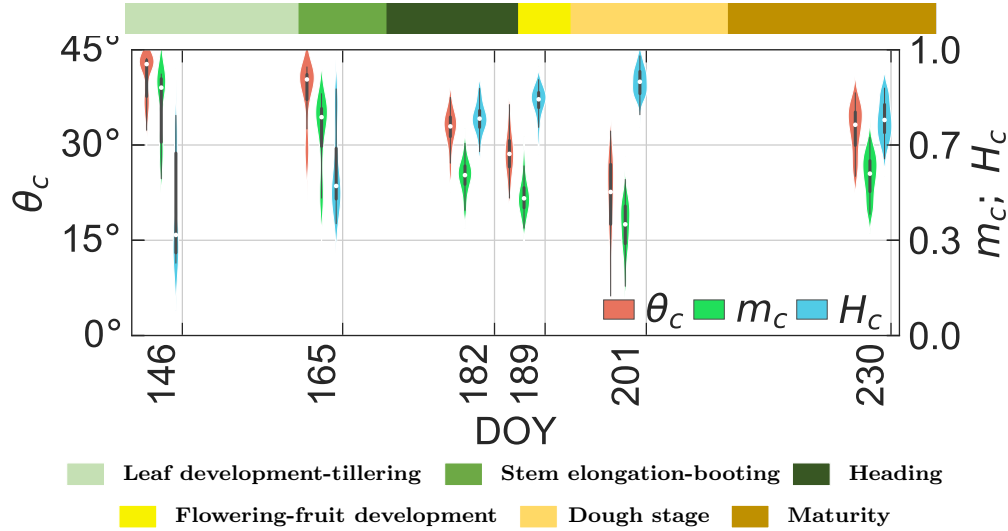


Figure 11: Temporal variation of m_c , H_c and θ_c for the growth stages of wheat. The white dot represents the median value, the black bar in the center represents the standard boxplot. On either side of the boxplot is a kernel density estimation displaying the shape of the data distribution.

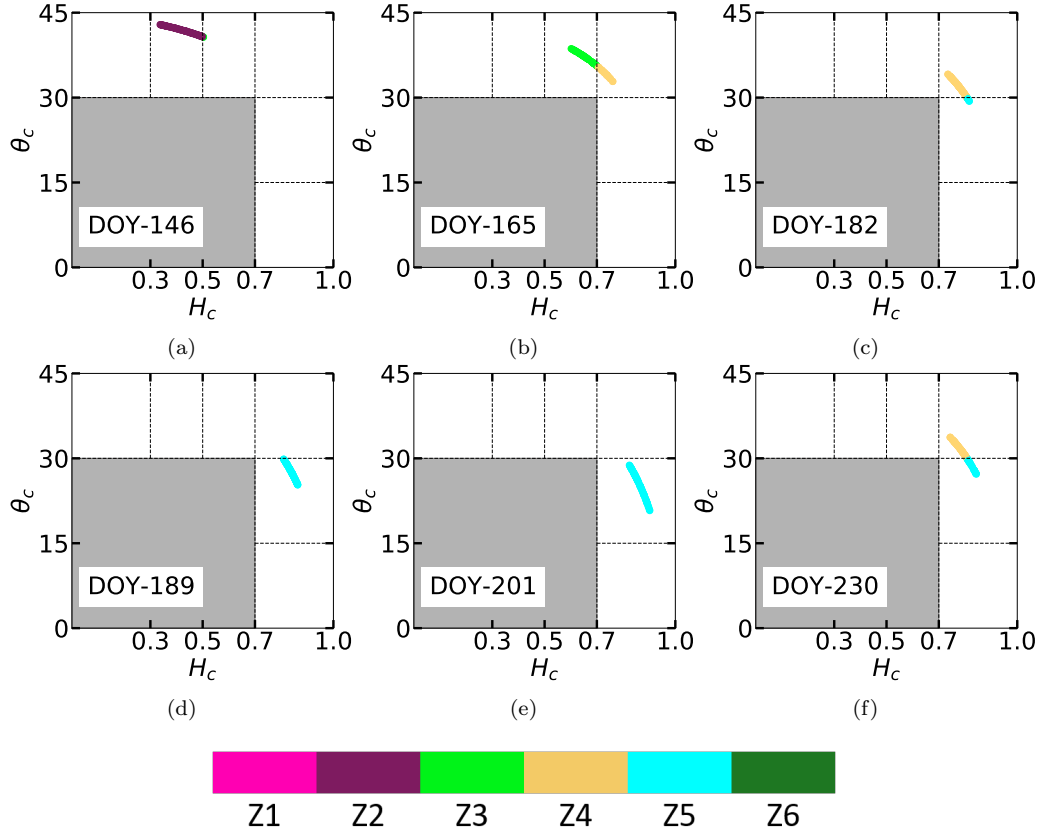


Figure 12: Temporal dynamics of the H_c/θ_c data cluster for wheat during entire growth period.

397 We have shown the temporal dynamics of the parameters m_c , H_c and θ_c
398 using a series of standard violin plots. The width of the violin represents the
399 probability that the sampling points portion will take on the given value. We
400 can observe from Figure 11 that m_c , H_c and θ_c are sensitive to wheat morpho-
401 logical changes. For example, we note that during the early leaf development
402 stage (around DOY-146), m_c and θ_c show differential scattering information
403 due to the presence of a minimal crop canopy. However, on DOY-201, wheat
404 has advanced to the dough stage and consequently, the interaction of the

405 radar wave with the matured canopy structure has increased. Therefore at
406 this stage, the increase in the cross-pol component has decreased the value
407 of m_c .

408 On DOY-146, high values of m_c and θ_c are evident from Figure 11, reach-
409 ing 0.8 ± 0.12 and $40.82^\circ \pm 3.41^\circ$, respectively. The distributions of m_c and
410 θ_c are left-skewed, indicating that most samples fall towards higher values
411 of m_c and θ_c . These high values correspond to pure scattering, which is due
412 to the dominance of the soil contribution relative to vegetation. As a result,
413 most data points are clustered in the low entropy pure scattering zone (Z2)
414 (Figure 12a). However, it is noteworthy that a fraction of the backscatter
415 response originates from the crop leaves and side tillers. The interaction of
416 radar waves with these structures has produced a small cluster with $\approx 11\%$
417 of data points in the medium entropy zone (Z3) (Table. 8).

418 We note that a few fields have advanced to the tillering stage during this
419 period due to early sowing. Hence, new tillers in those fields might have
420 decreased m_c and increased H_c . During stem elongation and booting, on
421 DOY-165, we observe a decrease in m_c and θ_c . The values of m_c and θ_c are
422 0.71 ± 0.12 and $37.87^\circ \pm 4.88^\circ$, respectively. This decrease is likely due to
423 changes in crop morphology in the vertical direction, with an increase in the
424 main stem and side tillers (Figure 2b). The distributions of m_c and θ_c have
425 shifted towards lower values. However, depending on the difference in the
426 growth pattern, bi-modal distributions of m_c and θ_c are observed.

427 During this period, high crop canopy density enhances scattering entropy,
428 shifting the data points towards medium to high entropy zones (Z3, and Z4)
429 as shown in Figure 12b. Hence, 57.7% of the data points are clustered within

the medium entropy zone, while 42.3 % are clustered within the high entropy zone (Table 8). Subsequently, during the heading stage (DOY-182), we observe a considerable drop in the mean values of m_c and θ_c from Figure 11. These values decrease by 21.13 % and 14.21 %, respectively, when compared to the previous date.

On DOY-182, the crops are in their advanced vegetative stage. The radar response is similar for all fields due to their comparable scattering randomness. The standard deviations of the sample distributions have decreased significantly. During this period, we observe from Figure 12c a shift in the data clusters from the medium entropy (Z3) to the high entropy zone (Z4). This shift could be due to changes in the wheat canopy structure during the heading stage. At this stage, the distribution of plant biomass shifts towards the upper layer of the canopy. Thus, a major contribution of scattering is from the upper canopy layer. A small proportion of data points ($\approx 15\%$) are clustered in the vegetation scattering zone (Z5) (Table. 8), which might be due to early flowering of these wheat fields.

With the advancement of wheat phenology to flowering stage (Figure 2d) on DOY-189, we observe a further drop in m_c (0.49 ± 0.06) and θ_c ($28.72^\circ \pm 3.39^\circ$). During this period, the wheat canopy forms a complex structure due to the appearance of flowers on the upper portion of the canopy layer. Interestingly, randomness in scattering during the flowering stage is more noticeable in the distribution of θ_c values. Moreover, the tail of the distribution becomes more comprehensive than the previous growth stage (Figure 11). The spread in the distribution of θ_c indicates multiple scattering mechanisms. Moreover, the shape of the distribution for m_c is almost equivalent

455 to θ_c , with an overall shift towards lower values. An increase in pseudo en-
 456 tropy has displaced the H_c/θ_c cluster towards the high entropy vegetation
 457 scattering zone (Z5) as shown in Figure 12d.

458 Dough and maturity stages continued from late July (DOY-201) to mid-
 459 August (DOY-225) with the values of m_c , and θ_c reaching their minimum
 460 when the crop advanced from flowering to early dough on DOY-201. The
 461 mean values of m_c and θ_c reach 0.38 ± 0.09 and $21.56^\circ \pm 6.24^\circ$ respectively.
 462 We observe a broad spread of θ_c values in Figure 11, which may be due
 463 to randomly oriented wheat stems and heads (Figure 2e). Wu et al. (1985)
 464 reported a similar phenomenon given that during the heading stage, a sig-
 465 nificant portion of the total scattering occurs from the wheat heads. It is
 466 noteworthy that the distributions are bi-modal, denoting two primary scat-
 467 tering sources: the thick upper canopy layer and the relatively less dense
 468 bottom canopy. We observe that all data points cluster in the high entropy
 469 and vegetation scattering zone (Z5) in the H_c/θ_c plot (Figure 12e).

Table 8: Temporal variation in the percentage of data points in each zone for different phenology stages of wheat. The zone with the maximum number of points at a particular phenology stage is highlighted in bold. Each row represents a phenology stage, and the solid line in between two phenology stages represents a significant variation in the temporal trend for the zones.

DOY	Z1	Z2	Z3	Z4	Z5	Z6	Growth stage
146	0.0	89.4	10.6	0.0	0.0	0.0	Leaf Development-Tillering
165	0.0	0.0	57.7	42.3	0.0	0.0	Stem Elongation-Booting
182	0.0	0.0	0.0	84.6	15.4	0.0	Heading
189	0.0	0.0	0.0	0.0	100	0.0	Flowering-Fruit development
201	0.0	0.0	0.0	0.0	100	0.0	Dough stage
230	0.0	0.0	0.0	65.4	34.6	0.0	Maturity

470 During the ripening stage, the canopy moisture content drops rapidly.
471 As a result, penetration of the SAR signal into the crop canopy increases
472 and hence, there is a substantial scattering contribution from the ground
473 to the total backscatter. A trend reversal is observed for all the dual -
474 polarimetric descriptors when the crop reaches the early mature stage (DOY-
475 230). During this period, the mean values of m_c and θ_c increase to $0.56 \pm$
476 0.07 and $32.54^\circ \pm 3.65^\circ$, respectively. The median of the distribution shifts
477 towards higher values (Figure 12f). We observe a decrease in the spread of
478 distributions for both m_c and θ_c in Figure 11 indicating uniformity in the
479 scattering mechanism.

480 A decrease in scattering entropy shifts the H_c/θ_c cluster towards the dis-
481 tributed scattering zone (Z4) from random scattering, as shown in Figure 12f.
482 However, 34.6 % of the data points are clustered within the vegetation scat-
483 tering zone (Z5) with 65.4 % of the data points clustered in Z4 (Table 8). The
484 Z5 clusters appearance might be due to the late maturity of wheat, which is
485 also in agreement with the bi-modal distribution of the m_c and θ_c parameters
486 in Figure 11.

487 The proportion of data points over different scattering regions for other
488 crop phenological stages is presented in Table 8. The results indicate a
489 smooth transition of scattering mechanisms throughout the growing cycle of
490 wheat. Using the proposed scattering descriptors and the novel clustering
491 framework, we capture different scattering mechanisms at each wheat growth
492 stage.

4.2.2. Canola

This section analyses the temporal characteristics of m_c , H_c and θ_c for different phenological stages of canola. In total, 48 sampling points in three canola fields (Field no. 206, 208, and 224) are used to assess the temporal dynamics of these parameters. We also evaluate the temporal variations of the H_c/θ_c cluster according to canola phenology.

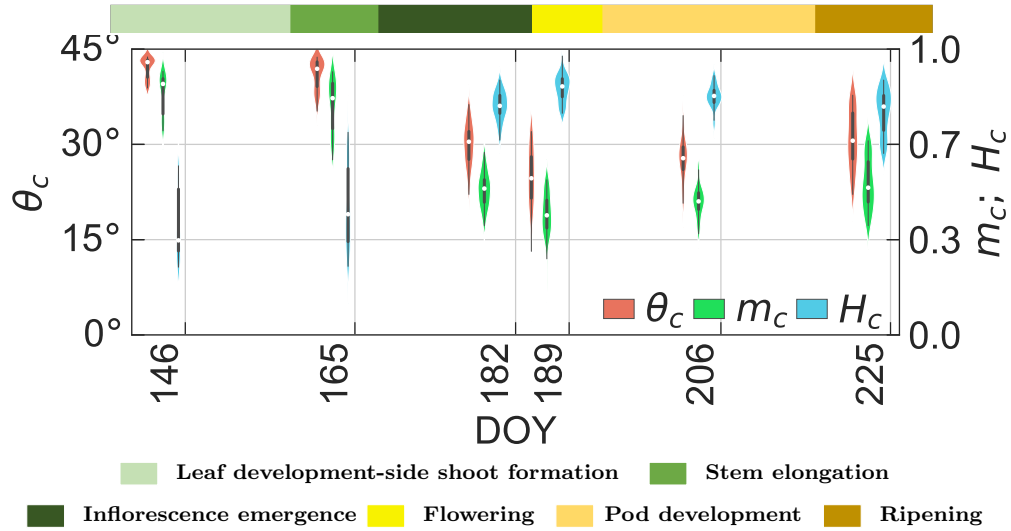


Figure 13: Temporal variation of m_c , H_c and θ_c for the growth stages of canola. The white dot represents the median value, the black bar in the center represents the standard boxplot. On either sides of boxplot is a kernel density estimation to show the distribution shape of the data.

498

Canola is a broadleaf crop with a distinctive canopy structure at every growth stage (McNairn et al., 2018; Mandal et al., 2020b). The seeding of the canola crop was completed by mid-May, as indicated in the in-situ data. Until the beginning of June, the plant advanced to its vegetative growth stage. The plant develops a dense rosette of leaves near the soil surface during the leaf development, as evident from Figure 3a. However, the size of

504

505 these leaves is comparable to the wavelength of the C-band (≈ 5.6 cm).

506 On DOY-146, the mean value of $\theta_c \approx 40^\circ$ and $m_c \approx 0.8$ which indicate
 507 dominant scattering from exposed soil due to sparse vegetation cover (Fig-
 508 ure 13). In Figure 14a, we observe that a majority of data points are clustered
 509 in zone Z2, which is characterized by medium entropy pure scattering. A few
 510 data points are in the medium to high entropy distributed scattering zone
 511 (Z3) as this crop advances to the leaf development stage.

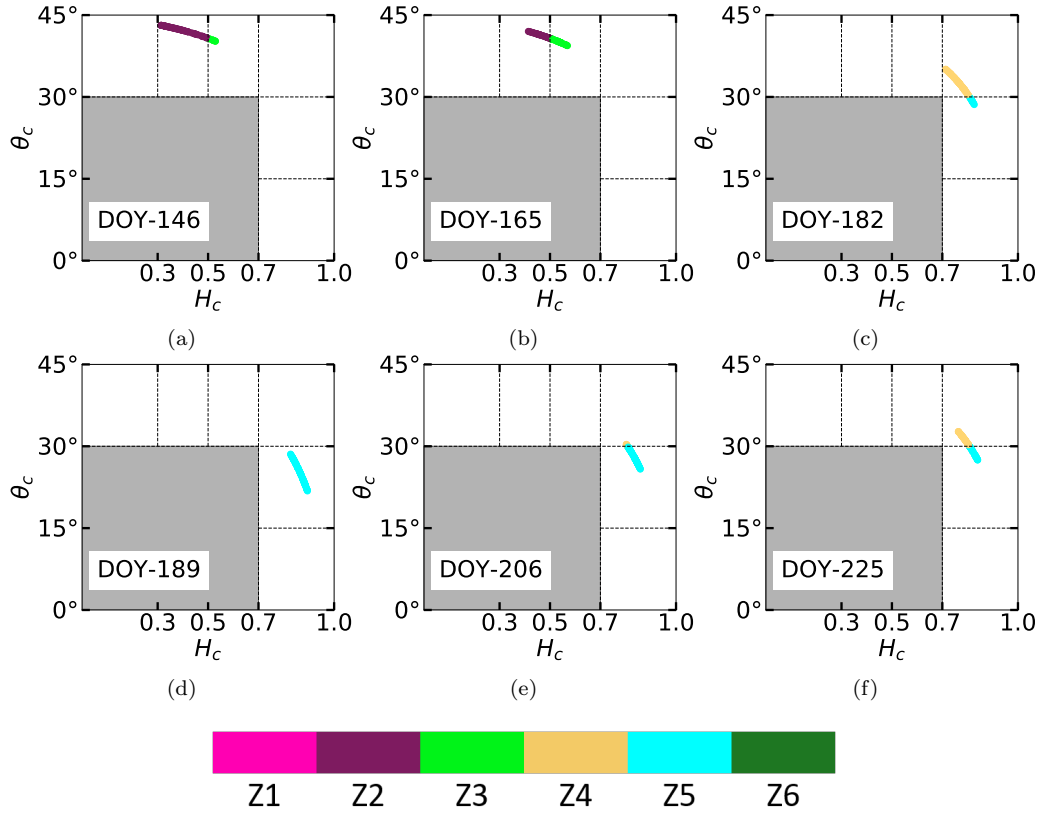


Figure 14: Temporal dynamics of the H_c/θ_c data cluster for canola during entire growth period.

512 As growth progresses to stem elongation, a noteworthy change into a

vertical plant structure can be observed from Figure 3b. At this stage, the attenuation of V-polarized waves increases. Further, an increase in biomass and PAI due to increased leaf density and branch formation leads to increased scattering randomness. On DOY-165, the H_c/θ_c cluster shifts from the pure (Z2) to the distributed scattering zone (Z3) due to a substantial amount of m_c component during stem elongation. The accumulation of points has increased in the distributed scattering zone (Z3) due to the matured crop morphology.

During inflorescence emergence (Figure 3c), flower buds develop and leaf density increases significantly. Consequently, we observe a change in the data cluster on DOY-182 (Figure 14c). Further, the values of m_c and θ_c dropped to 0.51 ± 0.06 and $29.94^\circ \pm 3.38^\circ$, respectively. On the other hand, the formation of branches increases scattering entropy. Hence, a shift in the H_c/θ_c cluster from medium entropy zone (Z3) to high entropy zone (Z4) is evident on DOY-182 (Figure. 14c).

During the flowering stage, the buds develop into flowers, and the main stem and branches grow (Figure 3d). On DOY-189, the scattering mechanism of all the data points is shifted towards high entropy vegetation scattering zone (Z5) (Figure 14d). We may attribute this shift to the development of a complex canopy geometry during the flowering and early pod development stage. As pods form, the canopy drops leaves. The decline of leaf cover followed by the development of pods dramatically changes the crop geometry. The canopy architecture becomes more random, with pods creating needle-like structures oriented randomly.

During the development of pods canola develops a dense, random canopy

structure. Hence, the mean values of m_c (0.47 ± 0.06) and θ_c ($27.6^\circ \pm 3.36^\circ$) are minimum on DOY-206. A majority of data points ($\approx 91\%$) are clustered into the high entropy vegetation scattering zone (Z5). At the same time, a small percentage ($\approx 9\%$) of data points are clustered into Z4 (Figure 14e). This small cluster may reflect the change in crop morphology as leaf area declines and the SAR signal interacts more with the needle-like canopy (Figure 3e).

Table 9: Temporal variation in the percentage of data points in each zone for different phenology stages of canola. The zone with the maximum number of points at a particular phenology stage is highlighted in bold. Each row represents a phenology stage and the solid line in between two phenology stages represents a significant variation in the temporal trend for the zones.

DOY	Z1	Z2	Z3	Z4	Z5	Z6	Growth stage
146	0.0	89.8	10.2	0.0	0.0	0.0	Leaf Development Side shoot formation
165	0.0	48.9	51.1	0.0	0.0	0.0	Stem Elongation
182	0.0	0.0	0.0	84.1	15.9	0.0	Inflorescence Emergence
189	0.0	0.0	0.0	0.0	100	0.0	Flowering
206	0.0	0.0	0.0	9.1	90.9	0.0	Pod Development
225	0.0	0.0	0.0	54.5	45.5	0.0	Ripening

Subsequently on DOY-225, we observe an increase in m_c and θ_c values to 0.53 ± 0.09 and $30.8^\circ \pm 4.63^\circ$, respectively. This increase in the values of the descriptors might be due to the decrease in overall canopy moisture content at maturity. As canopy moisture declines, the SAR signal can penetrate deeper into the crop canopy. Hence, at late maturity, there might be a greater contribution from the soil. Because of these physical changes, the H_c/θ_c

550 cluster shifts towards the distributed scattering zone (Z4) (Figure 14f). The
 551 bi-modal distribution of the parameters m_c and θ_c (Figure 13) indicates two
 552 major sources of scattering. In particular, some fraction of the crop may be
 553 entering the mid/end-ripening stage, resulting in higher values of m_c and θ_c .
 554 In contrast, other canopies may be just entering early ripening, resulting in
 555 lower values. We observe this difference in Figure 14f. Notably, 54.5 % of
 556 the data points fall in distributed scattering zone (Z4), whereas 45.5 % of
 557 the data points are in the vegetation scattering zone (Z5). The proportion
 558 of data points over different scattering regions for all phenological stages
 559 of canola is presented in Table 9. The results indicate a smooth transition
 560 of scattering mechanisms throughout the growing cycle. Consequently, the
 561 proposed descriptors exhibit high sensitivity to the phenological stages of
 562 both wheat and canola. Hence, these descriptors are useful in monitoring
 563 phenological changes for both crops.

564 5. Conclusion

565 In this study, we propose three polarimetric descriptors from dual-pol
 566 Sentinel-1 (S1) GRD SAR data. These parameter are: the pseudo scattering-
 567 type parameter (θ_c), the co-pol purity parameter (m_c), and the pseudo scat-
 568 tering entropy parameter (H_c). We have expressed these descriptors in terms
 569 of $q = \sigma_{XY}^\circ / \sigma_{XX}^\circ$, with $0 \leq q \leq 1$. Additionally, we have proposed a novel
 570 unsupervised clustering framework using θ_c and H_c .

571 We have used the dual-pol descriptors and the novel clustering framework
 572 to analyze temporal growth dynamics of wheat and canola over a Canadian
 573 test site. The results are very encouraging in assessing crop dynamics for

574 different major phenological stages. The high sensitivity of these descriptors
575 to different crop growth stages is evident in this context.

576 In the scope of this study, we have characterized diverse crop phenolog-
577 ical stages in terms of the physical scattering of the electromagnetic wave
578 from targets using the GRD SAR data. The unsupervised clustering frame-
579 work using H_c/θ_c contains six zones representing different physical scattering
580 mechanisms. Hence, it provides essential information about the crop growth
581 stages without any *a priori* knowledge and therefore very useful in interpret-
582 ing the available radar data.

583 The temporal analysis of the proposed descriptors revealed their high sen-
584 sitivity across different phenology stages of wheat and canola. The dynamic
585 range of θ_c from leaf development to fruit development of wheat is 41° to
586 21.6° . Similarly, the variations of m_c and H_c are 0.8 to 0.38 and 0.35 to 0.9,
587 respectively. Similar dynamic ranges of these parameters are also evident for
588 canola crop. Furthermore, the proposed clustering schema efficiently cap-
589 tured the diverse phenology stage of wheat and canola. For leaf development
590 and tillering stages of wheat, 90 % of the sampling points are clustered into
591 low to medium entropy pure scattering zone. During flowering and fruit de-
592 velopment stages, 100 % of the sampling points are shifted into high entropy
593 vegetation scattering zone. Subsequently, during the maturity stage, the
594 clusters of the sampling points were split between the high entropy vegeta-
595 tion scattering and high entropy distributed scattering zones with $> 65\%$ of
596 the sampling points in the high entropy distributed scattering zone. Similar
597 cluster dynamics are observed for the canola crop.

598 However, it is computationally intensive to implement these algorithms

599 for a high volume of temporal data from a global agricultural monitoring
600 perspective. To overcome this limitation, we utilized the cloud-based plat-
601 form (GEE) to acquire and process the dense time-series data of Sentinel-1.
602 Implementing the algorithms in GEE also facilitates efficient generation of
603 global maps of crop phenology stages.

604 This study only used the GRD SAR data product to formulate the target
605 characterizing descriptors demonstrating promising results for natural tar-
606 gets. We can further extend this study to different crop types and different
607 dual-pol SAR sensors configurations. The proposed descriptors should be
608 beneficial in studying natural ecosystems with upcoming dual-pol NASA-
609 ISRO Synthetic Aperture Radar Mission (NISAR) and Sentinel SAR con-
610 stellation.

611 **Acknowledgement**

612 The authors are grateful to the SMAPVEX16 science team for providing
613 ground truth information. The authors would like to thank the Google Earth
614 Engine team for providing the free SAR data processing platform. Authors
615 also acknowledge the GEO-AWS Earth Observation Cloud Credits Program,
616 which supported the computation with Sentinel-1 on AWS cloud platform
617 through the project: “AWS4AgriSAR-Crop inventory mapping from SAR
618 data on a cloud computing platform”, and formed the testbed for processing
619 pipelines. Mr. Narayanarao B. and Mr. Subhadip Dey would like to ac-
620 knowledge the support from the Ministry of Education (formerly Ministry of
621 Human Resource and Development-MHRD), Govt. of India, towards their
622 doctoral research work. The authors want to thank the support of the Span-

ish Ministry of Science and Innovation, State Research Agency (AEI) and the European Regional Development Fund under project TEC2017-85244-C2-1-P. The authors are thankful to the overleaf team (<https://overleaf.com/>) for providing the latex editing platform.

References

- Agriculture, M., B., 2016. Agriculture Province of Manitoba. URL: <https://www.gov.mb.ca/agriculture/crops/seasonal-reports/crop-report-archive/index.html>.
- Ainsworth, T., Kelly, J., Lee, J.S., 2009. Classification comparisons between dual-pol, compact polarimetric and quad-pol SAR imagery. *ISPRS Journal of Photogrammetry and Remote Sensing* 64, 464–471.
- Ainsworth, T.L., Kelly, J., Lee, J.S., 2008. Polarimetric analysis of dual polarimetric SAR imagery, in: 7th European Conference on Synthetic Aperture Radar, VDE. pp. 1–4.
- Ali, I., Naeimi, V., Cao, S., Elefante, S., Bauer-Marschallinger, B., Wagner, W., 2017. Sentinel-1 data cube exploitation: Tools, products, services and quality control, in: *Proc. Big Data Space*, pp. 40–43.
- Arias, M., Campo-Bescós, M.Á., Álvarez-Mozos, J., 2020. Crop classification based on temporal signatures of sentinel-1 observations over navarre province, Spain. *Remote Sensing* 12, 278.
- Bargiel, D., 2017. A new method for crop classification combining time

644 series of radar images and crop phenology information. Remote sensing of
645 environment 198, 369–383.

646 Bhuiyan, H.A., McNairn, H., Powers, J., Friesen, M., Pacheco, A., Jack-
647 son, T.J., Cosh, M.H., Colliander, A., Berg, A., Rowlandson, T., et al.,
648 2018. Assessing SMAP soil moisture scaling and retrieval in the Carman
649 (Canada) study site. Vadose Zone Journal 17, 1–14.

650 Bicout, D., Brosseau, C., 1992. Multiply scattered waves through a spa-
651 tially random medium: entropy production and depolarization. Journal
652 de Physique I 2, 2047–2063.

653 Bousbih, S., Zribi, M., Lili-Chabaane, Z., Baghdadi, N., El Hajj, M., Gao, Q.,
654 Mougenot, B., 2017. Potential of Sentinel-1 radar data for the assessment
655 of soil and cereal cover parameters. Sensors 17, 2617.

656 Brisco, B., Brown, R., Gairns, J., Snider, B., 1992. Temporal ground-based
657 scatterometer observations of crops in western Canada. Canadian journal
658 of remote sensing 18, 14–21.

659 Brosseau, C., 1991. Polarization transfer and entropy transformation. Optik
660 (Stuttgart) 88, 109–117.

661 Cloude, S., 2007. The dual polarization entropy/alpha decomposition: A
662 palsar case study. ESASP 644, 2.

663 Cloude, S., 2009. Polarisation: applications in remote sensing. OUP Oxford.

664 Cloude, S.R., Pottier, E., 1997. An entropy based classification scheme for

land applications of polarimetric sar. IEEE transactions on geoscience and remote sensing 35, 68–78.

Davidson, M.W., Le Toan, T., Mattia, F., Satalino, G., Manninen, T., Borgeaud, M., 2000. On the characterization of agricultural soil roughness for radar remote sensing studies. IEEE Transactions on Geoscience and Remote Sensing 38, 630–640.

De Bernardis, C.G., Vicente-Guijalba, F., Martinez-Marin, T., Lopez-Sanchez, J.M., 2015. Estimation of key dates and stages in rice crops using dual-polarization SAR time series and a particle filtering approach. IEEE Journal of Selected Topics in Applied Earth Observations and Remote Sensing 8, 1008–1018.

Della Vecchia, A., Ferrazzoli, P., Guerriero, L., Ninivaggi, L., Strozzi, T., Wegmuller, U., 2008. Observing and modeling multifrequency scattering of maize during the whole growth cycle. IEEE Transactions on Geoscience and Remote Sensing 46, 3709–3718.

Dey, S., Bhattacharya, A., Ratha, D., Mandal, D., Frery, A.C., 2020a. Target characterization and scattering power decomposition for full and compact polarimetric SAR data. IEEE Transactions on Geoscience and Remote Sensing .

Dey, S., Bhattacharya, A., Ratha, D., Mandal, D., McNairn, H., Lopez-Sanchez, J.M., Rao, Y., 2020b. Novel clustering schemes for full and compact polarimetric SAR data: An application for rice phenology char-

acterization. ISPRS Journal of Photogrammetry and Remote Sensing 169,
135–151.

ESA, 2017. Sen4cap - Sentinels for common agriculture policy. [http://
esa-sen4cap.org/](http://esa-sen4cap.org/).

Ferrazzoli, P., Paloscia, S., Pampaloni, P., Schiavon, G., Solimini, D., Coppo,
P., 1992. Sensitivity of microwave measurements to vegetation biomass and
soil moisture content: A case study. IEEE Transactions on Geoscience and
Remote Sensing 30, 750–756.

Fikriyah, V.N., Darvishzadeh, R., Laborte, A., Khan, N.I., Nelson, A., 2019.
Discriminating transplanted and direct seeded rice using Sentinel-1 inten-
sity data. International Journal of Applied Earth Observation and Geoin-
formation 76, 143–153.

Gorelick, N., Hancher, M., Dixon, M., Ilyushchenko, S., Thau, D., Moore,
R., 2017. Google earth engine: Planetary-scale geospatial analysis for
everyone. Remote sensing of Environment 202, 18–27.

Hariharan, S., Mandal, D., Tirodkar, S., Kumar, V., Bhattacharya, A.,
Lopez-Sanchez, J.M., 2018. A novel phenology based feature subset selec-
tion technique using random forest for multitemporal PolSAR crop classi-
fication. IEEE Journal of Selected Topics in Applied Earth Observations
and Remote Sensing 11, 4244–4258.

Hird, J.N., DeLancey, E.R., McDermid, G.J., Kariyeva, J., 2017. Google
earth engine, open-access satellite data, and machine learning in support
of large-area probabilistic wetland mapping. Remote sensing 9, 1315.

- 710 Homayouni, S., McNairn, H., Hosseini, M., Jiao, X., Powers, J., 2019. Quad
711 and compact multitemporal C-band PolSAR observations for crop charac-
712 terization and monitoring. *International Journal of Applied Earth Obser-*
713 *vation and Geoinformation* 74, 78–87.
- 714 Jackson, K.R., Ramakrishnan, L., Muriki, K., Canon, S., Cholia, S., Shalf,
715 J., Wasserman, H.J., Wright, N.J., 2010. Performance analysis of high
716 performance computing applications on the amazon web services cloud, in:
717 2010 IEEE second international conference on cloud computing technology
718 and science, IEEE. pp. 159–168.
- 719 Jiao, X., Kovacs, J.M., Shang, J., McNairn, H., Walters, D., Ma, B., Geng,
720 X., 2014. Object-oriented crop mapping and monitoring using multi-
721 temporal polarimetric RADARSAT-2 data. *ISPRS Journal of Photogram-*
722 *metry and Remote Sensing* 96, 38–46.
- 723 Kumar, P., Prasad, R., Gupta, D., Mishra, V., Vishwakarma, A., Yadav,
724 V., Bala, R., Choudhary, A., Avtar, R., 2018. Estimation of winter wheat
725 crop growth parameters using time series Sentinel-1A SAR data. *Geocarto*
726 *international* 33, 942–956.
- 727 Kussul, N., Lemoine, G., Gallego, F.J., Skakun, S.V., Lavreniuk, M., She-
728 lestov, A.Y., 2016. Parcel-based crop classification in Ukraine using
729 Landsat-8 data and Sentinel-1A data. *IEEE Journal of Selected Topics*
730 *in Applied Earth Observations and Remote Sensing* 9, 2500–2508.
- 731 Lasko, K., Vadrevu, K.P., Tran, V.T., Justice, C., 2018. Mapping double
732 and single crop paddy rice with Sentinel-1A at varying spatial scales and

733 polarizations in Hanoi, Vietnam. *IEEE journal of selected topics in applied*
734 *earth observations and remote sensing* 11, 498–512.

735 Lee, J.S., Grunes, M.R., Pottier, E., 2001. Quantitative comparison of clas-
736 sification capability: Fully polarimetric versus dual and single-polarization
737 sar. *IEEE Transactions on Geoscience and Remote Sensing* 39, 2343–2351.

738 Li, H., Zhang, C., Zhang, S., Atkinson, P.M., 2019. Full year crop monitoring
739 and separability assessment with fully-polarimetric L-band UAVSAR: A
740 case study in the Sacramento Valley, California. *International Journal of*
741 *Applied Earth Observation and Geoinformation* 74, 45–56.

742 Lopez-Sanchez, J.M., Cloude, S.R., Ballester-Berman, J.D., 2012. Rice phe-
743 nology monitoring by means of SAR polarimetry at X-band. *IEEE Trans-*
744 *actions on Geoscience and Remote Sensing* 50, 2695–2709.

745 Lopez-Sanchez, J.M., Vicente-Guijalba, F., Ballester-Berman, J.D., Cloude,
746 S.R., 2014. Polarimetric response of rice fields at C-band: Analysis and
747 phenology retrieval. *IEEE Transactions on Geoscience and Remote Sensing*
748 52, 2977–2993.

749 Mandal, D., Kumar, V., Bhattacharya, A., Rao, Y.S., Siqueira, P., Bera,
750 S., 2018. Sen4Rice: A processing chain for differentiating early and late
751 transplanted rice using time-series Sentinel-1 SAR data with Google Earth
752 Engine. *IEEE Geoscience and Remote Sensing Letters* 15, 1947–1951.

753 Mandal, D., Kumar, V., Lopez-Sanchez, J.M., Bhattacharya, A., McNairn,
754 H., Rao, Y., 2020a. Crop biophysical parameter retrieval from Sentinel-1

755 SAR data with a multi-target inversion of Water Cloud Model. Interna-
756 tional Journal of Remote Sensing 41, 5503–5524.

757 Mandal, D., Kumar, V., Ratha, D., Dey, S., Bhattacharya, A., Lopez-
758 Sanchez, J.M., McNairn, H., Rao, Y.S., 2020b. Dual polarimetric radar
759 vegetation index for crop growth monitoring using sentinel-1 SAR data.
760 Remote Sensing of Environment 247, 111954.

761 Mascolo, L., Lopez-Sanchez, J.M., Vicente-Guijalba, F., Nunziata, F., Migli-
762 accio, M., Mazzarella, G., 2016. A complete procedure for crop phenology
763 estimation with PolSAR data based on the complex Wishart classifier.
764 IEEE Transactions on Geoscience and Remote Sensing 54, 6505–6515.

765 McNairn, H., Brisco, B., 2004. The application of C-band polarimetric SAR
766 for agriculture: A review. Canadian Journal of Remote Sensing 30, 525–
767 542.

768 McNairn, H., Jiao, X., Pacheco, A., Sinha, A., Tan, W., Li, Y., 2018. Esti-
769 mating canola phenology using synthetic aperture radar. Remote Sensing
770 of Environment 219, 196–205.

771 McNairn, H., Tom, J., Powers, J., Bélair, J., Berg, A., Bullock, A., Collian-
772 der, A., Cosh, A., Kim, M., Ramata, S., et al., 2016. Experimental plan
773 SMAP validation experiment 2016 in Manitoba, Canada (SMAPVEX16-
774 MB).

775 Minasny, B., Shah, R.M., Che Soh, N., Arif, C., Indra Setiawan, B., et al.,
776 2019. Automated Near-Real-Time Mapping and Monitoring of Rice Ex-
777 tent, Cropping Patterns, and Growth Stages in Southeast Asia Using

778 Sentinel-1 Time Series on a Google Earth Engine Platform. Remote Sens-
779 ing 11, 1666.

780 Nasrallah, A., Baghdadi, N., El Hajj, M., Darwish, T., Belhouchette, H.,
781 Faour, G., Darwich, S., Mhawej, M., 2019. Sentinel-1 data for winter
782 wheat phenology monitoring and mapping. Remote Sensing 11, 2228.

783 Nelson, A., Setiyono, T., Rala, A.B., Quicho, E.D., Raviz, J.V., Abonete,
784 P.J., Maunahan, A.A., Garcia, C.A., Bhatti, H.Z.M., Villano, L.S., et al.,
785 2014. Towards an operational SAR-based rice monitoring system in Asia:
786 Examples from 13 demonstration sites across Asia in the RIICE project.
787 Remote Sensing 6, 10773–10812.

788 Nemani, R., Votava, P., Michaelis, A., Melton, F., Milesi, C., 2011. Col-
789 laborative supercomputing for global change science. Eos, Transactions
790 American Geophysical Union 92, 109–110.

791 Nguyen, D.B., Gruber, A., Wagner, W., 2016. Mapping rice extent and
792 cropping scheme in the Mekong Delta using Sentinel-1A data. Remote
793 Sensing Letters 7, 1209–1218.

794 Periasamy, S., 2018. Significance of dual polarimetric synthetic aperture
795 radar in biomass retrieval: An attempt on Sentinel-1. Remote Sensing of
796 Environment 217, 537–549.

797 Ratha, D., Mandal, D., Kumar, V., McNairn, H., Bhattacharya, A., Frery,
798 A.C., 2019. A generalized volume scattering model-based vegetation index
799 from polarimetric SAR data. IEEE Geoscience and Remote Sensing Letters
800 16, 1791–1795.

801 Redkar, T., Guidici, T., Meister, T., 2009. Windows azure platform.
802 Springer.

803 Sarabandi, K., 1991. Electromagnetic scattering from vegetation canopies. .

804 Schlund, M., Erasmi, S., 2020. Sentinel-1 time series data for monitoring the
805 phenology of winter wheat. *Remote Sensing of Environment* 246, 111814.

806 Singha, M., Dong, J., Zhang, G., Xiao, X., 2019. High resolution paddy
807 rice maps in cloud-prone Bangladesh and Northeast India using Sentinel-1
808 data. *Scientific data* 6, 1–10.

809 Song, Y., Wang, J., 2019. Mapping winter wheat planting area and monitor-
810 ing its phenology using Sentinel-1 backscatter time series. *Remote Sensing*
811 11, 449.

812 Steele-Dunne, S.C., McNairn, H., Monsivais-Huertero, A., Judge, J., Liu,
813 P.W., Papathanassiou, K., 2017. Radar remote sensing of agricultural
814 canopies: A review. *IEEE Journal of Selected Topics in Applied Earth*
815 *Observations and Remote Sensing* 10, 2249–2273.

816 Trudel, M., Charbonneau, F., Leconte, R., 2012. Using RADARSAT-2 po-
817 larimetric and ENVISAT-ASAR dual-polarization data for estimating soil
818 moisture over agricultural fields. *Canadian Journal of Remote Sensing* 38,
819 514–527.

820 Ulaby, F., 1975. Radar response to vegetation. *IEEE Transactions on An-*
821 *tennas and Propagation* 23, 36–45.

- 822 Ulaby, F.T., El-Rayes, M.A., 1987. Microwave dielectric spectrum of
823 vegetation-Part II: Dual-dispersion model. *IEEE Transactions on Geo-*
824 *science and Remote Sensing* , 550–557.
- 825 Van Tricht, K., Gobin, A., Gilliams, S., Piccard, I., 2018. Synergistic use of
826 radar Sentinel-1 and optical Sentinel-2 imagery for crop mapping: a case
827 study for Belgium. *Remote Sensing* 10, 1642.
- 828 Vreugdenhil, M., Wagner, W., Bauer-Marschallinger, B., Pfeil, I., Teubner,
829 I., Rüdiger, C., Strauss, P., 2018. Sensitivity of Sentinel-1 backscatter to
830 vegetation dynamics: An Austrian case study. *Remote Sensing* 10, 1396.
- 831 Wali, E., Tasumi, M., Moriyama, M., 2020. Combination of Linear Regression
832 Lines to Understand the Response of Sentinel-1 Dual Polarization SAR
833 Data with Crop Phenology—Case Study in Miyazaki, Japan. *Remote*
834 *Sensing* 12, 189.
- 835 Wang, H., Magagi, R., Goïta, K., Trudel, M., McNairn, H., Powers, J., 2019.
836 Crop phenology retrieval via polarimetric sar decomposition and random
837 forest algorithm. *Remote Sensing of Environment* 231, 111234.
- 838 Whelen, T., Siqueira, P., 2018. Time-series classification of Sentinel-1 agri-
839 cultural data over North Dakota. *Remote sensing letters* 9, 411–420.
- 840 Wiseman, G., McNairn, H., Homayouni, S., Shang, J., 2014. RADARSAT-
841 2 polarimetric SAR response to crop biomass for agricultural production
842 monitoring. *IEEE Journal of Selected Topics in Applied Earth Observa-*
843 *tions and Remote Sensing* 7, 4461–4471.

⁸⁴⁴ Wu, L.k., Moore, R.K., Zoughi, R., 1985. Sources of scattering from vege-
⁸⁴⁵ tation canopies at 10 Ghz. IEEE Transactions on Geoscience and Remote
⁸⁴⁶ Sensing , 737–745.